Research Article | Vol. 30, No. 6 / 14 Mar 2022 / Optics Express 9193
Optics EXPRESS

Compact thin film lithium niobate folded intensity modulator using a waveguide crossing

SEAN NELAN,[1,2,*] ANDREW MERCANTE,[2] COOPER HURLEY,[1] SHOUYUAN SHI,[1,2] PENG YAO,[2] BENJAMIN SHOPP,[2] AND DENNIS W. PRATHER[1,2]

[1]School of Electrical and Computer Engineering, University of Delaware, Newark, Delaware 19716, USA
[2]Phase Sensitive Innovations, Newark, Delaware 19713, USA
[*]snelan@udel.edu

Abstract: A small footprint, low voltage and wide bandwidth electro-optic modulator is critical for applications ranging from optical communications to analog photonic links, and the integration of thin-film lithium niobate with photonic integrated circuit (PIC) compatible materials remains paramount. Here, a hybrid silicon nitride and lithium niobate folded electro-optic Mach Zehnder modulator (MZM) which incorporates a waveguide crossing and 3 dB multimode interference (MMI) couplers for splitting and combining light is reported. This modulator has an effective interaction region length of 10 mm and shows a DC half wave voltage of roughly 4.0 V, or a modulation efficiency ($V\pi \cdot L$) of roughly 4 V·cm. Furthermore, the device demonstrates a power extinction ratio of roughly 23 dB and shows .08 dB/GHz optical sideband power roll-off with index matching fluid up to 110 GHz, with a 3-dB bandwidth of 37.5 GHz.

1. Introduction

As the need for small footprint, higher-bandwidth, low latency and low loss data communication grows, so too does the need to develop technology which will help us realize these needs [1,2]. Here, the optical modulator is an integral part of active and passive millimeter wave imaging systems, modern telecommunications networks and data communication, and is widely used in on-chip RF photonic devices, frequency comb generation, on chip signal splitting, sensing, and quantum photonics [1–12]. The ideal optical modulator must use a PIC-compatible material system, maintain a small device footprint, and boast an ultra-wide RF bandwidth [13–17]. Silicon (Si) free carrier plasma dispersion-based modulation has been investigated due to its low-cost complimentary metal-oxide semiconductor (CMOS)-compatible fabrication process and excellent scalability, but is inherently limited in extinction ratio and bandwidth [18–20]. Si-based modulation is further limited by its low second-order non-linearity, intrinsic absorption loss, third-order non-linearity, narrow transmission spectrum, and unwanted dopant diffusion at high temperatures [15,18]. Some of these issues can be overcome through the integration of organic electro-optic materials with the Si platform, but the organic nature of this platform does not lend itself to long-term environmental stability [21–23]. The ideal platform for a low-voltage, high-bandwidth and environmentally-stable modulator should show a strong electro-optic (Pockels) effect, and a linear response to an applied modulation voltage. As such, the Si-based free carrier plasma dispersion-based modulation platform is ruled out in favor of lithium niobate-based modulation [4,16]. Lithium niobate ($LiNbO_3$) offers an extremely strong second-order non-linearity ($\chi^{(2)}$) and as such a strong linear electro-optic effect, exceptionally low optical absorption across a wide range of wavelengths, pure phase modulation, zero chirping and stability at high temperatures. Moreover, $LiNbO_3$ boasts a third-order non-linearity ($\chi^{(3)}$) which is three magnitudes lower than Si. Legacy, or bulk $LiNbO_3$ modulators may use titanium (Ti)-diffused waveguides to guide an optical mode, but in turn suffer poor optical confinement ($\Delta n < 0.02$)

#453050 https://doi.org/10.1364/OE.453050
Journal © 2022 Received 5 Jan 2022; revised 8 Feb 2022; accepted 24 Feb 2022; published 4 Mar 2022

Optics EXPRESS

resulting in a large mode size requiring any metal electrodes to be placed far from the waveguide to avoid incurring metal absorption losses. Consequentially, the half-wave voltage ($V\pi$) and the minimum optical bending radius of the device is greatly increased. Bulk $LiNbO_3$ modulators then have large footprints and high power requirements. A typical bulk $LiNbO_3$ modulator brings a $V\pi$·L of 12-32 V·cm [14]. However, these limitations can be overcome using modulators made with crystal ion sliced (CIS) films of $LiNbO_3$ on insulator (TFLNOI), which guide optical modes almost 20 times smaller than their bulk-$LiNbO_3$ counterparts [13,14,17,24,25]. Now, the electrodes can be placed closer to the optical waveguide, leading to enhanced modulation efficiency, lower noise and power consumption, and PIC-compatibility. These devices can support bending radii near 250 μm, compared to roughly 1 cm on bulk $LiNbO_3$ devices [14]. Ultra-wide bandwidth, high efficiency low loss modulators have been demonstrated in the TFLNOI material system through ridge-etched or strip-loaded waveguides [13,15,17,25,26]. To ensure compatibility with current CMOS silicon-based processes, silicon nitride (SiN_x) was chosen as the ideal candidate for hybrid integration. SiN_x shares a similar refractive index to $LiNbO_3$, and has low propagation loss across a wide range of optical wavelengths [11,27–30]. SiN_x also features a low second-order non-linearity, small thermo-optic coefficient, high-power handling ability, is PIC compatible and can be easily grown or deposited using either plasma enhanced chemical vapor deposition (PECVD) or low pressure chemical vapor deposition (LPCVD) [15,29,30]. Finally, the use of 100nm thick SiN strip-loaded waveguides rather than ridge-etched TFLN waveguides, or 220nm thick SiN strip-loaded waveguides as shown in previous work opens the door to the possibility of a low-loss waveguide coupler at the end facet, which will be presented in future work [14]. In previous work, a sub-1-volt $V\pi$ modulator in the hybrid thin film $LiNbO_3$-SiN_x material platform has been demonstrated [14].

With this in mind, we must also consider the packaging and size of the device. A standard push-pull electro-optic modulator utilizes a straight waveguide before and after the interaction region, where light enters one side of the device and exits another [14]. This requires fiber coupling to both sides of the device simultaneously, and greatly increases the overall size and complexity of the system. Instead, the device can be "folded," or bent back on itself. Here, a 180° bend is introduced to the waveguides and electrodes to direct the signal back towards the input. Now, the physical length of the device is nearly halved with no consequences to modulation efficiency, bandwidth, or power requirements. A folded modulator can be used with a single v-groove array (VGA), and only requires the polishing and preparation of one end-facet. This scheme greatly reduces the footprint of the device if it were to be used in a PIC. Moreover, multiple folds can be incorporated to achieve a longer interaction region with no impact on physical device length Fig. 1(e). This layout may help to reduce the size of a standalone packaged device. This does, however introduce some challenges to the design and fabrication of the modulator. If a standard MZM were to be bent back on itself such that the interaction regions before and after the bend were the same length, the latter region would reverse any effects that the first region might have had, because the polarity of the modulating electric field interacting with the mode inside the $LiNbO_3$ is now the inverse of what it was during the first half of the modulator. To overcome this, we have crossed both waveguides of the interaction region under the 180° bend in the electrodes. Now, both sections before and after the bend will contribute to the total modulation of the device. Moreover, the optical path length of both arms, and the optical vs. electrical path length is matched to allow high speed operation without RF and optical field separation.

In this work, a high-speed folded hybrid $LiNbO_3$-SiN_x electro-optic MZM using a waveguide crossing to facilitate a true push-pull scheme throughout both interaction regions is demonstrated. To the best of our knowledge, this is the first time a high-speed folded $LiNbO_3$-SiN_x electro-optic MZM using a waveguide crossing has been designed, simulated and characterized in this material platform. The fabricated device saw a measured DC-$V\pi$ of roughly 4.0 V with a 10 mm interaction

Optics EXPRESS

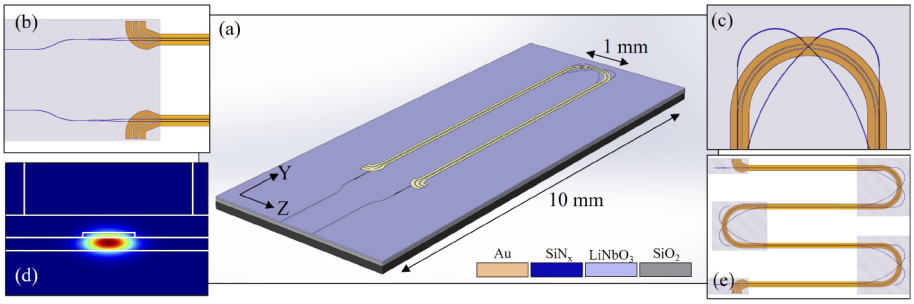

Fig. 1. (a) Aerial view of the folded modulator with waveguide crossing. (b) Aerial view of the MMI and probing region. Electrodes are transparent for viewing. Shaded areas represent SiO_2 protection region. (c) Aerial view of the waveguide crossing region. Electrodes are transparent for viewing. Shaded areas represent SiO_2 protection region. (d) Simulated TE optical mode profile at one arm of the modulator, where the lateral mode is guided by a 100 nm x 2 μm SiN_x loading strip, and optical wavelength is 1550 nm. (e) Aerial view of a possible layout incorporating three folds. Shaded areas represent SiO_2 protection region. Not to scale.

region, and a power extinction ratio of roughly 23 dB. Finally, the device achieved a frequency roll-off of roughly 0.08 dB/GHz with UV15 index matching fluid, and an optical propagation loss of 0.66 dB/cm.

2. Design and simulation

2.1. Device layout

The 3D aerial view of the folded electro-optic modulator with a waveguide crossing is shown in Fig. 1(a). The cross section of the device is shown in Fig. 4(d). The material stack, from top to bottom, is comprised of a 500 nm buffer layer of PECVD SiO_2, 100 nm of PECVD SiN_x deposited on 300 nm X-cut thin-film $LiNbO_3$, which is bonded to a 4.7 μm SiO_2 layer (T_{BBUF}), atop a 500 μm Si handle. To confine the first order transverse electric (TE) mode, the width (W_{SiN}) and thickness (T_{SiN}) of the strip-loaded SiN_x waveguide is chosen to be 2 μm and 100 nm, respectively.

With this, the simulated bending loss for a 500 μm radius bend is <.01 dB/cm, or <0.01 dB/90° bend. The optical TE mode profile in one of the modulator arms is shown in Fig. 1(d). Here, the mode confinement in the $LiNbO_3$ is roughly 69.5 %. The optical TE mode profile of the 1x2 multi-mode interference (MMI) splitter is shown in Fig. 2(d).

The folded modulator uses a push-pull MZM configuration both before and after the fold. The device is fed through a single waveguide which directs the signal into a 1x2 splitter to equally split the signal into two arms. Both arms pass under a short section of 2 μm thick SiO_2 while the optical signal travels under a 90° bend in the probing section of the electrodes, introduced to simplify the probing of the device during testing and operation. The electrodes are configured in a ground-signal-ground (GSG) push-pull configuration, and apply an opposite electric field to each arm. Here, there is a 500 nm SiO_2 buffer layer (T_{BUF}) under the electrodes to prevent metal absorption losses from occurring, as demonstrated in 4(d). In this configuration, a π/2-phase shift is required to produce a total π-phase shift upon recombination at the end of the interaction region, which halves the total Vπ of the device. After the initial 5 mm interaction region, the oxide buffer thickness is again increased from 500 nm to 2 μm. This ensures no metal absorption loss is incurred when the optical waveguides pass under the metal electrodes in the waveguide crossing section, shown in Fig. 1(c). The optical waveguides cross directly under the signal electrode, such that the optical and RF path lengths are maintained, and the optical path length of

Optics EXPRESS

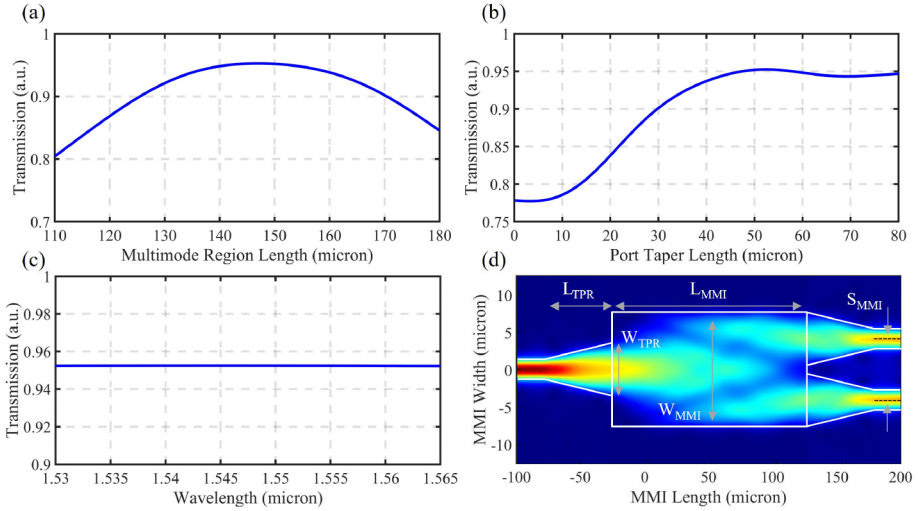

Fig. 2. (a) Simulated combined transmitted power in both output arms of the MMI as the length of the multimode region (L_{MMI}) is swept from 110 to 180 μm. Here, the input and output waveguides are tapered. (b) Simulated combined transmitted power in both output arms of the MMI as the length section (L_{TPR}) at the input and output is swept from 0 to 80 μm. (c) Simulated combined transmitted power in both output arms of the MMI as the input wavelength is swept from 1.53 to 1.565 μm across the optical c-band. (d) Aerial view of the mode profile within the MMI with dimensions defined. Here, L_{TPR} = 52.5 μm while L_{MMI} = 148 μm.

both modulation arms is matched. The waveguide arms then enter the second 5 mm interaction region, identical to the first. Finally, both arms enter a 2x1 MMI splitter which recombines the light to produce an intensity-modulated signal. The optical mode propagates in the Y-crystal direction, while the electrodes are placed such that the RF field is polarized in the +/- Z-crystal direction, where the maximum r_{33} = 31 pm/V coefficient is achieved for the TE optical mode [11,14,28,31].

2.2. MMI design

An MMI splitter and combiner are used as 3 dB couplers to achieve the folded MZM configuration. While directional couplers and Y-splitters are extremely sensitive to fabrication tolerance and waveguide dimensions, the MMI offers a greater fabrication tolerance, as well as large bandwidth and polarization insensitivity [14,32]. After the fiber coupling facet at the input of the device, the signal travels through an optical S-bend with radius 500 μm and into a 1x2 MMI, which is used to split the optical signal into each modulation arm. Following modulation, the two arms are again recombined using a 2x1 MMI. The signal is then sent through another identical S-bend which reduces the waveguide pitch to 750 μm to accommodate the VGA used for coupling. An MMI operates based on a principle of self-imaging. An input field is reconstructed periodically after a certain propagation distance. Consequentially, the length (L_{MMI}) of the 1x2 MMI must be designed and chosen such that the input field is reconstructed into two output fields at the end of the device. The width of the MMI must also be considered to avoid unwanted evanescent coupling of the output fields after the multimode region. The width of the MMI is then set to 15 μm, which yields a mode separation distance (S_{MMI}) of 8 μm when the second order TE mode in the multimode region is excited. The self-imaging property of a multimode waveguide can be used to estimate the initial length required for the multimode region of the MMI [32]. The initial length of the MMI region is found using the 2D mathematical approximation given by L_{MMI}

Optics EXPRESS

$= \frac{3\pi}{8(\beta_0-\beta_1)}$ [14,32]. β_0 and β_1 are defined as the propagation constants of the two lowest order modes inside the multimode region, with $\beta = n_{\text{eff}}\frac{2\pi}{\lambda}$. The n_{eff} of the lowest order TE modes in the MMI region are found to be 2.205635, and 2.207614, respectively, using Lumerical's MODE solver.

We find that the length given by the approximation is 146.9 μm. Linear tapers at the input and output waveguides of length (L_{TPR}) 52.5 μm and width (W_{TPR}) 7 μm are introduced to broaden the allowable fabrication tolerance and increase overall bandwidth [33]. Lumerical's MODE simulation software is used to optimize the design parameters. Both W_{MMI} = 15 μm and S_{MMI} = 8 μm are fixed, and L_{MMI} is swept from 110 μm to 180 μm and plotted against the total combined transmission to find the optimized final length of the MMI, Fig. 2(a).

The simulation shows maximum transmission at L_{MMI} = 148 μm, with L_{TPR} being 52.5 μm. While this is near the length given by the self-imaging solution, the introduction of linear tapers at the input and output waveguides of the MMI has an effect on the overall length of the cavity to properly reconstruct the image at the output waveguides. Because this MMI is symmetrically fed, the input power should be equally split among the output arms barring any fabrication intolerance. This also holds true upon recombination at the end of the modulation region due to the reciprocal nature of the MMI splitter/combiner [14,32,33]. Here, each input arm will contribute equally to the power of the output mode. That is, if each input arm shares the same phase, there will be total constructive interference at the output port, whereas if an additional π phase-difference is introduced to the arms through modulation, there will be total destructive interference. This is the basis for a push-pull intensity modulator.

2.3. Waveguide crossing design

The waveguide crossing implemented in this device is of straightforward design. Here, the two arms of the modulator, waveguides of dimension 2 μm x 100 nm, are crossed perpendicularly under the bent portion of the electrodes. There is an additional SiO_2 buffer thickness introduced on top of the waveguide crossing to eliminate any optical absorption loss that may result from the optical mode passing under the Au electrodes. The crossing must effectively transmit the optical signal to the port directly opposite its input port. If there should be any power leakage to the adjacent, or crossing ports, the extinction ratio of the device will suffer.

The correct operation of the waveguide crossing is verified using Lumerical's Finite-Difference Time-Domain (FDTD) simulation software. In Fig. 3(a), the transmitted power in the through-port of the waveguide crossing is plotted as a function of input wavelength. The wavelength is swept from 1.53 to 1.565 μm, covering the optical c-band. Throughout the range, there is less than 0.01 dB transmission loss. Next, the same simulation is run for the cross-ports of the waveguide crossing, shown in Fig. 3(b). There is negligible transmission throughout the band, with a transmission peak of -111.5 dB at 1.565 μm. The structure and mode-field propagation from left to right of the crossing is shown in Fig. 3(d).

2.4. High-speed electrode design

The ground-signal-ground (GSG) configured electrodes must be designed such that the device maintains a 50 Ω impedance at high frequencies with minimal RF absorption or conduction loss to minimize reflections in the feed network. The width of the electrode gap (W_{GAP}) in the interaction region must be kept as small as possible to maximize RF and optical field overlap, and maintain low-voltage operation [14]. However, too small, or a misaligned gap will contribute to increased absorption loss due to the optical mode interacting with the electrode. In Fig. 3(b), the optical absorption loss is plotted as the electrode gap is swept from 3 to 10 μm using Lumerical MODE simulation software. W_{GAP} is chosen to be 6.5 um which yields minimal optical absorption loss. The width of the ground electrodes (W_{GND}) is set as 50 μm, and the height of the Au electrodes (T_{ELEC}) is 1.8 μm to ensure compatibility with a laser writing and electroplating process. With

Optics EXPRESS

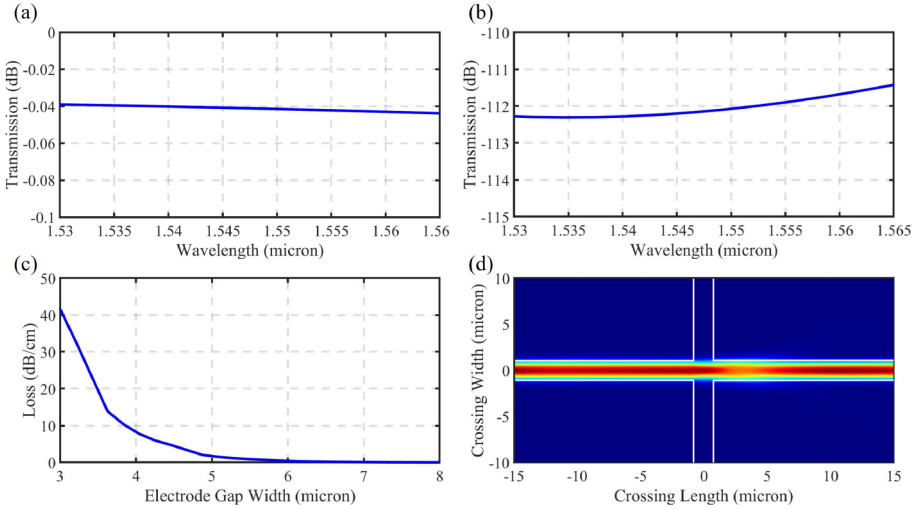

Fig. 3. (a) Simulated transmitted power in the through-port of the waveguide crossing as the input wavelength is swept from 1.53 to 1.565 μm across the optical c-band. (b) Simulated transmitted power in in one cross-port of the waveguide crossing as the input wavelength is swept from 1.53 to 1.565 μm across the optical c-band. (c) Simulated optical absorption loss in the waveguide passing between the electrodes in the interaction region as the electrode gap (W_{GAP}) is swept from 3 to 8 μm. (d) Aerial view of the mode profile within the waveguide crossing. The mode is propagating from left to right.

these parameters, Ansys High Frequency Simulation Software (HFSS) is used to find the optimal electrode signal width (W_{SIG}). In Fig. 4(c), the RF impedance from 0 to 67 GHz is plotted with W_{SIG} = 22.5 μm, which yields roughly 50 Ω throughout the higher frequencies. The electrode contains one interaction region before and after the folded region, each 5 mm long. For a driving voltage of 1 V between the signal and ground electrodes, a peak field of roughly 1.5 x 10^5 V/m is observed. The simulated RF index (n_{RF}) is plotted in Fig. 4(a), and converges to roughly 1.92 above 20 GHz. The simulated S-parameters are plotted in Fig. 4(b). The simulated impedance is plotted in Fig. 4(c).

Both the beginning and end of the GSG electrode is tapered outward and then bent at 90° to allow for probing of the device using a GSG probe. An additional 1500 nm SiO_2 cladding is introduced in this section for a total of 2 μm to allow the waveguide to pass under the electrode without incurring additional absorption loss. The impedance of the tapered section must also be considered. Here, the width of the ground electrode in the probe region (W_{PGND}) and the width of the signal electrode in the probing region (W_{PSIG}) are driven by the required width and pitch to use a GSG probe. W_{PGND} is set to 75 μm, while W_{PSIG} is set to 70 μm, so that a GSG probe with an 80 to 100 μm pitch can be used. HFSS is used to determine the appropriate electrode gap in the probing region (W_{PGAP}). W_{PGAP} is chosen to be 14 μm. The length of the electrodes is set at 10mm to maintain a high operational bandwidth and a low-Vπ [34].

The simulated optical group index (n_{Og}) of the fundamental TE mode is found to be 2.21, while the group index of the RF mode in the electrodes (n_{RF}) is 1.94.

Optics EXPRESS

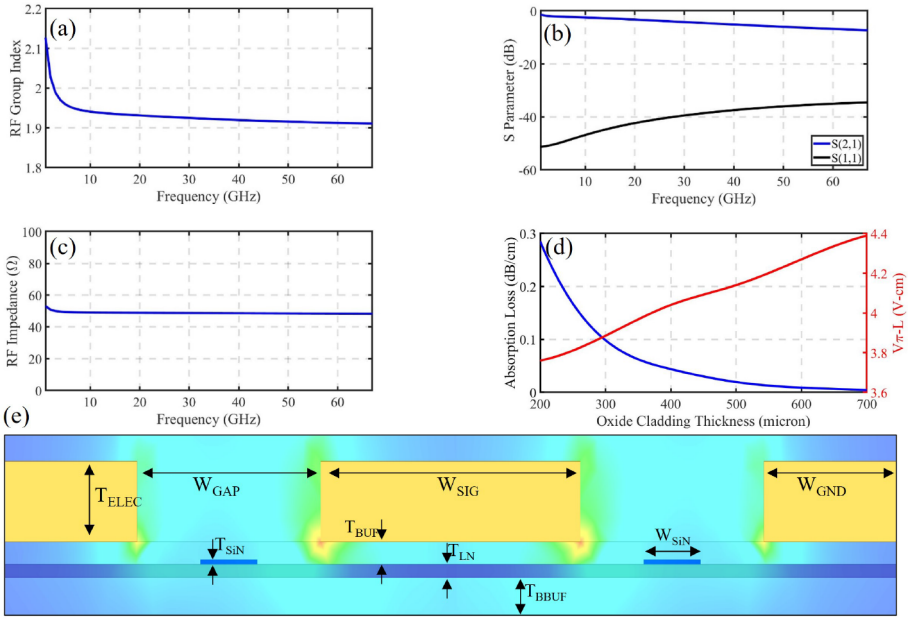

Fig. 4. (a) Simulated RF group index of the coplanar-waveguide (CPW) GSG electrodes from 0 to 67 GHz. (b) Simulated S-parameters of the 2-port CPW GSG electrodes from 0 to 67 GHz. (c) Simulated RF impedance of the CPW GSG electrodes from 0 to 67 GHz. (d) Simulated optical metal absorption loss and simulated DC Vπ-L vs SiO_2 buffer thickness under Au electrodes when W_{GAP} is 6.5 μm. (e) Cross-sectional view of the electric field concentration within the device layer structure. Dimensions are defined.

3. Fabrication

Fabrication of the folded modulator begins on a 300 nm thick X-cut TFLNOI substrate procured from NanoLN^{TM}. There is a 4.7 μm layer of thermal SiO_2 below the $LiNbO_3$, which is bonded to a 500 μm thick Si handle. A 100 nm thick layer of TiW (10%/90%) is sputtered on top of the thin film $LiNbO_3$ using an Angstrom metal sputtering system. A layer of negative electron-beam resist is spun on to the sample, and a Raith EBPG5200+ is used to pattern alignment structures via electron-beam lithography for future lithographic steps. The metal alignment structures are then defined via dry etching in a Plasma-Therm Apex SLR fluorine ICP. After a thorough clean, a 100 nm thick layer of SiN_x is deposited on top of the thin film $LiNbO_3$ using plasma-enhanced chemical vapor deposition (PECVD) in a PD-220N PECVD system. This layer covers and protects the metal markers, and will be used to define the SiN_x strip-loaded waveguides. The refractive index for the SiN_x is 1.943 at 1550 nm. A negative electron-beam resist is again spun onto the sample, and used to define the optical structures via electron-beam lithography using a Raith EBPG5200+. The negative resist serves as an etch mask to define the features via dry etching of the SiN_x layer in a fluorine ICP. A 2 μm SiO_2 buffer layer is then deposited using PECVD. A layer of SU8 2002 photoresist (Kayaku Advanced Materials, Inc) is spun onto the sample, and a laser writer is used to pattern the regions where an increased thickness of the SiO_2 buffer layer will protect the optical mode from interacting with an overhead Au electrode. The rest of the SiO_2 buffer layer is reduced to 500 nm thickness via dry etching. To reduce RF absorption losses, the device is annealed in an O_2 environment. A metal layer stack of TiW, Au and TiW is deposited onto the sample using an Angstrom metal sputtering system to form the electrode seed layer for electroplating. A thick layer of PMMA positive electron-beam resist

Optics EXPRESS

is spun onto the sample and used to pattern the metal electrodes via electron-beam lithography with a Raith EBPG5200+. An electroplating process is then used to realize the 1.8 μm thick Au electrodes. Finally, the device's waveguide facets are polished to increase fiber coupling efficiency. Microscopic and scanning electron microscope (SEM) images of the fabricated folded modulator are depicted in Fig. 5. A complete flow of the fabrication steps is found in Fig. 6.

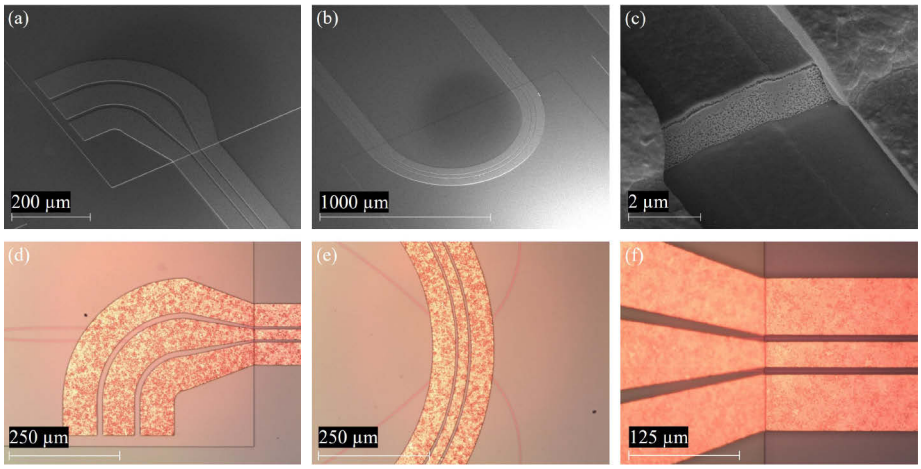

Fig. 5. (a) SEM image of the RF-probing region at the beginning and end of the interaction regions. The probing region rests on an additional 1.5 μm of PECVD SiO_2. (b) SEM image of the RF and optical bending region. The bending region rests on an additional 1.5 μm of PECVD SiO_2. (c) A magnified view of the transition between the 500 nm SiO_2-clad interaction region and the 2 μm SiO_2-clad probing region. (d) An optical microscope view of the RF probing region. (e) An optical microscope view of the waveguide crossing under the RF bending region. (f) An optical microscope view of the transition between the 500 nm SiO_2-clad interaction region and the 2 μm SiO_2-clad probing region.

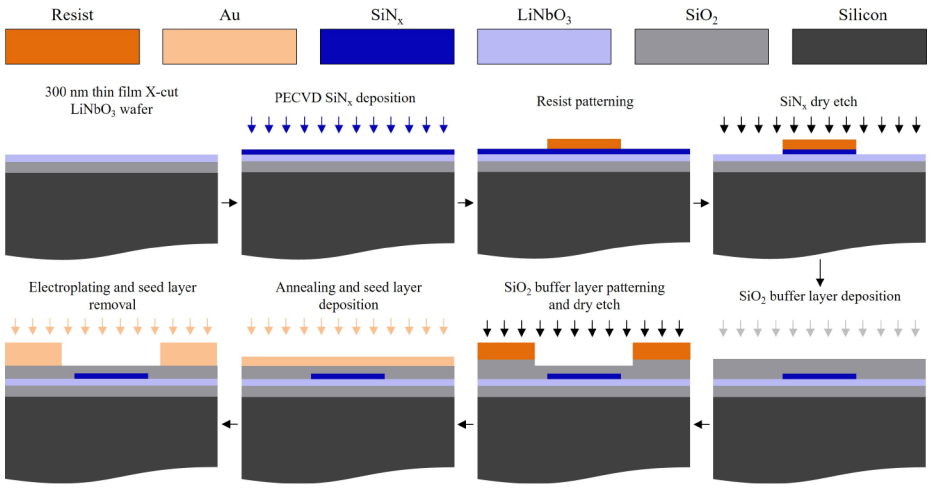

Fig. 6. Simplified fabrication flow chart of the folded SiN_x-$LiNbO_3$ modulator.

Optics EXPRESS

4. Optical and RF characterization

4.1. Optical characterization

To characterize the optical waveguides, waveguide crossing and MMI structures, a tunable telecom laser (Keysight 81608A) is set to a wavelength of 1550 nm. The output is then connected to an OZ Optics 1x2 lensed fiber array, with a Mode Field Diameter (MFD) of roughly 2.5 μm through a polarization-maintaining (PM) fiber patch cable. The light exiting the lensed fiber array is then free-space coupled to the waveguide end-facet of a test structure fabricated on the same layout. The structure's length is increased to provide clearer loss data. The output from the lensed fiber array is connected to a Thor Labs optical power meter which is used to ensure proper alignment of the array to the input and output waveguide. The device is then tuned to peak-bias. Now, the tunable laser source is replaced with a reflectometer/light-wave analyzer (Luna OBR 6415), and the optical back-reflection from the waveguide is measured near the middle of the modulator to determine the combined absorption loss and roughness induced back-scattering at each point along the structure. The waveguide roughness is found to be constant along the length of the waveguide. The data is processed to account for dispersion effects in the input fiber. In Fig. 8(d), it is shown that the device has an overall propagation loss of 0.66 dB/cm, where the MMIs and waveguide crossing have a negligible contribution to the overall loss. If the waveguide crossing were to greatly contribute to the overall loss of the device, a signal drop-off after roughly 26 mm would be present. The total insertion loss of the device is roughly 21.0 dB. The on-chip loss after the 52 mm path length is roughly 3.43 dB. This includes propagation loss, metal absorption loss, and loss due to the MMIs and waveguide crossing. Using the Lumerical MODE Solver, the simulated mode field power overlap of roughly 21% is shown between the waveguide and the lensed fiber array in Fig. 7. This accounts for 6.84 dB at each waveguide facet. Therefore, the additional loss is likely incurred due to the MFD mismatch between the lensed fiber and the waveguide at each end facet, accounting for roughly 8.75 dB each. The additional 1.95 dB loss per facet may be accounted for in any misalignment between the waveguide and the lensed fiber array. In future work, the coupling loss will be reduced by more closely matching the MFD of the input fiber and waveguide.

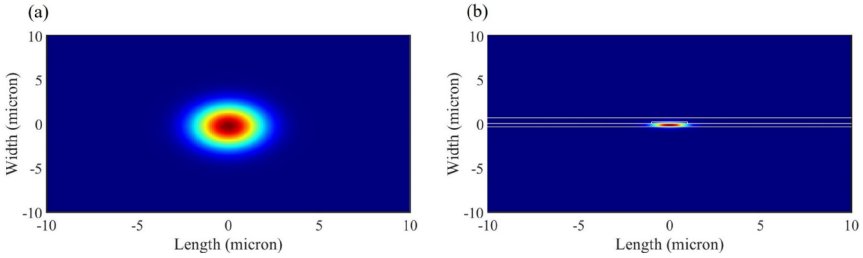

Fig. 7. (a) Simulated mode field of the OZ Optics lensed fiber array. Simulations done in Lumerical MODE Solver. (b) Simulated mode field of the waveguide. Simulations done in Lumerical MODE Solver.

4.2. Electro-optic characterization

The MZM functionality as an electro-optic (EO) transducer is characterized by measuring the Vπ of the device at low frequencies. Here, the observed Vπ is our chosen figure of merit. To demonstrate that the folded modulator with the waveguide crossing shows half of the measured Vπ of the folded modulator without a waveguide crossing with half the electrode interaction region, a low speed (150 kHz) triangular voltage wave is applied to the GSG electrodes using an arbitrary waveform generator (Agilent 33220A) via a 100 μm-pitch GSG probe. The push-pull

Optics EXPRESS

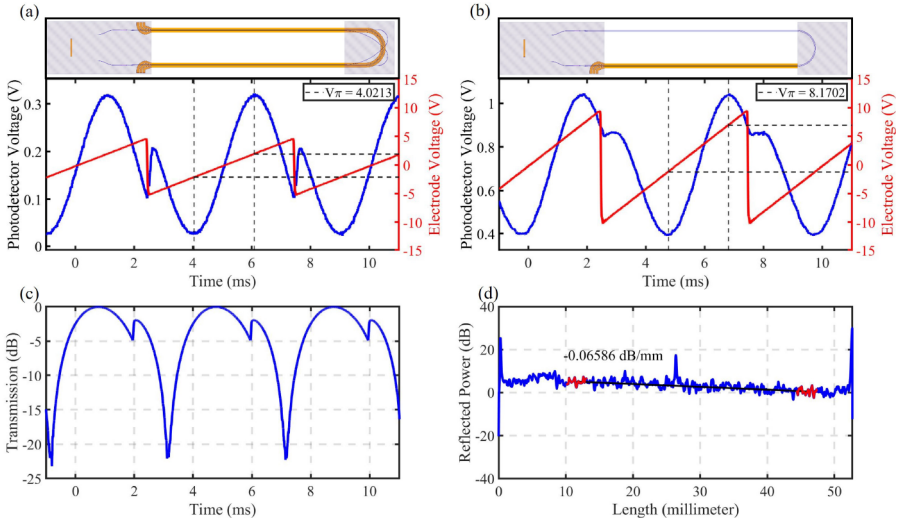

Fig. 8. (a) Measured Vπ of the 10 mm folded waveguide crossing modulator. Measured Vπ is roughly 4.02 V. Measurement taken at 150 kHz. (b) Measured Vπ of the 5 mm folded reference modulator. No waveguide crossing is present. Measured Vπ is roughly 8.17 V. Measurement taken at 150 kHz. (c) Measured extinction ratio of the 10 mm folded waveguide crossing modulator. Measured extinction ratio is roughly 23 dB. (d) Measured combined propagation loss and back-scatter of the on-chip reference structure. Measured propagation loss is 0.66 dB/cm.

electrodes are excited such that the center electrode is probed with a positive or negative voltage, while the outer electrodes are grounded. In this configuration, the first arm's phase change is complimentary to that of the second arm. The optical output signal is then connected to an InGaAs photodetector (DET01CFC), which is connected to an adjustable trans-impedance amplifier (TIA) (DHPCA-100) and fed to an oscilloscope (RTB2002). The output of the waveform generator and the photodetector are observed on the oscilloscope and presented in Fig. 8(a) and Fig. 8(b). The normalized optical transmission in a logarithmic scale is then plotted to find the static extinction ratio of the device, shown in Fig. 8(c). The measured Vπ of the 10 mm folded modulator with a waveguide crossing and the 5 mm folded modulator without crossing is roughly 4 V and roughly 8.2 V, respectively. The measured extinction ratio of the folded modulator with a waveguide crossing is roughly 23 dB, which is found by plotting the normalized optical transmission in the logarithmic scale. This demonstrates that the waveguide crossing is effective and does not have any leakage from its input to either adjacent port. If any leakage were present, the measured Vπ would be greater than half that of the 5 mm folded reference device, and the measured extinction ratio would suffer.

4.3. High frequency electrode characterization

The high frequency electrical response of the GSG electrodes was characterized through a 2-port measurement using a Keysight PNA-X network analyzer. Here, a 50 Ω high-frequency GSG probe with an operational bandwidth of 67 GHz is connected to each end of the GSG electrodes, and a frequency sweep performed from 10 MHz to 67 GHz. The data in Fig. 9. is extracted using the acquired real and imaginary S-parameter matrix at each frequency point. The S-parameters are shown in Fig. 9(a). There is an initial drop-off of roughly 2.4 dB at < 1 GHz due to high reflection from an impedance mismatch below the 10 MHz measurement threshold. From 1 GHz to 67 GHz, S(2,1) and S(1,2) fall only 6 dB, and is observed to be roughly -6.3 dB at the 40

Optics EXPRESS

GHz target frequency. There is a periodic resonance every 5 GHz seen in S(1,1) and S(2,2), which is expected for an electrode of total length 14 mm with an RF index near 1.94. This phenomena can be seen in the measured sideband power as well, in Fig. 9(d). The RF impedance is shown in Fig. 9(b), and is extracted from the measured real and imaginary S(1,1) parameter. The impedance trends slightly downwards throughout the measurement, but remains near 50 Ω. Because the impedance is extracted from the measured S-parameters, the observed resonance of the electrode is seen in the measured impedance. Finally, the RF index, extracted from the real and imaginary S(2,1) parameter is shown in Fig. 9(c). The RF index settles to roughly 1.94 at 20 GHz. The index mismatch between the optical and RF mode is then 0.27, with the RF mode propagating faster than the optical mode.

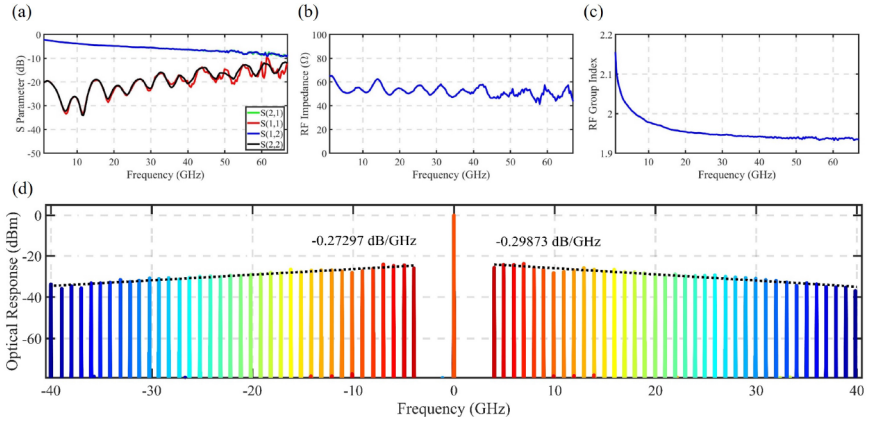

Fig. 9. (a) Measured S-parameters of the 2-port CPW GSG electrodes from 0 to 67 GHz. Extracted from the real and imaginary measured S-parameter matrix. (b) Measured RF impedance of the CPW GSG electrodes from 0 to 67 GHz. Extracted from the real and imaginary S(1,1) parameters. (c) Measured RF group index of the coplanar-waveguide (CPW) GSG electrodes from 0 to 67 GHz. Extracted from the real and imaginary S(2,1) parameters. (d) Measured optical sidebands at quadrature bias from 0 to 40 GHz using a 1550 nm wavelength carrier signal.

4.4. *High frequency optical characterization*

The high frequency electro-optic response of the MZM was characterized by measuring the optical sideband power with an RF modulating signal applied to the electrodes. A tunable telecom laser is used to launch 1550nm TE-polarized light into the folded MZM device, while an RF signal generated by a signal generator (Keysight MXG N5183) is connected to the input side of the GSG electrode through a 50 Ω high-frequency GSG probe with an operational bandwidth of 67 GHz. As such, the RF and optical signals are co-propagating. In this way, the overlap between the modulating RF field and the modulated optical signal is maintained for as long as possible. The modulator is biased to quadrature using a DC source to ensure the modulator is operating in the most linear region of the transmission curve. The RF modulating signal is swept from 1 to 40 GHz in 1 GHz increments, and the intensity of the sidebands of the modulated optical signal is observed using an APEX AP 2083A optical spectrum analyzer (OSA). The RF source is then connected to a Keysight thermocouple power meter (U8489A) and again swept from 1 to 40 GHz to gather the RF input power at each frequency step. The modulation spectrum is normalized to the optical carrier input, and the RF feed and insertion loss are accounted for. The modulation spectrum from 3 to 40 GHz at quadrature bias of the 10 mm device is shown in Fig. 9(d). Lower frequencies are omitted due to an unlevel power output from the MXG. The

Optics EXPRESS

sideband power roll-off from low frequencies to 40 GHz is roughly 0.3 dB/GHz. While the optical and RF path lengths are maintained, and the optical path length of both modulation arms is matched, a length mismatch may be introduced to maintain RF and optical mode overlap to increase 3-dB bandwidth. That is to say, the optical waveguide crossing could be positioned such that the optical distance is $\frac{1.94}{2.21}$ that of the RF distance.

In previous work [13,15], an index matching fluid has also been used to raise the RF index via application to the electrodes interaction region. The device is then measured to 110 GHz (Keysight PNA-X with N5295AX03 range extenders) with UV15 applied to the interaction region to more closely match the index of the RF and optical fields, demonstrated in Fig. 10(c). Here, the RF and optical group indices converge at 2.21; a near perfect match at RF frequencies above 40 GHz. While some additional RF loss is measured in Fig. 10(a), the index matching yields an extremely level sideband at frequencies up to 110 GHz, and demonstrates a 3-dB bandwidth of 37.5 GHz, Fig. 10(d). Here, the sideband power roll-off from low frequencies to 110 GHz is roughly 0.08 dB/GHz. The experimental test setup is shown in Fig. 11.

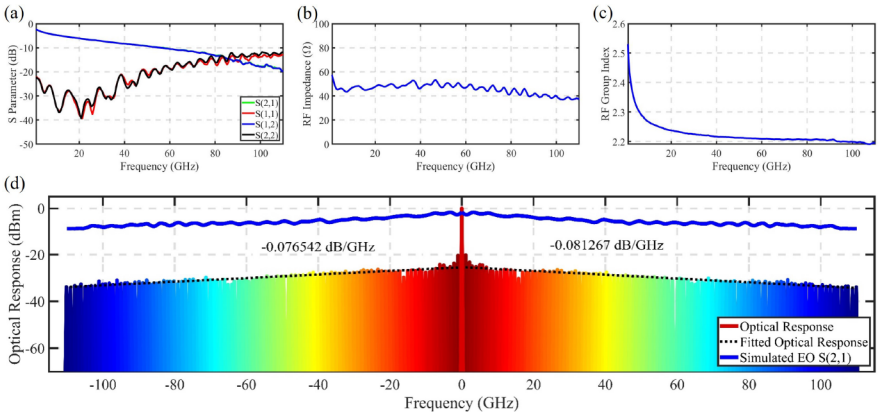

Fig. 10. (a) Measured S-parameters of the 2-port CPW GSG electrodes from 0 to 110 GHz with a UV15 coating. Extracted from the real and imaginary measured S-parameter matrix. (b) Measured RF impedance of the CPW GSG electrodes from 0 to 110 GHz with a UV15 coating. Extracted from the real and imaginary S(1,1) parameters. (c) Measured RF group index of the coplanar-waveguide (CPW) GSG electrodes from 0 to 110 GHz with a UV15 coating. Extracted from the real and imaginary S(2,1) parameters. (d) Measured optical sidebands and simulated electro-optic S(2,1) response from measured RF data at quadrature bias from 0 to 110 GHz using a 1550 nm wavelength carrier signal with a UV15 coating.

To further optimize the high-frequency performance of the device, capacitively-loaded traveling wave electrodes can be implemented to lower RF loss and closely match the RF and optical group velocities. This would eliminate the need for a UV15 index matching fluid as used in this device.

Optics EXPRESS

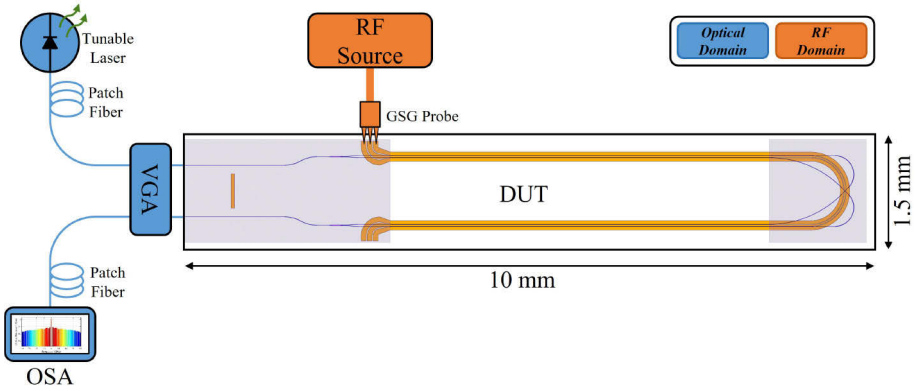

Fig. 11. Schematic of the experimental setup used to collect sideband data of the device.

5. Conclusion

In conclusion, a hybrid silicon nitride and lithium niobate folded electro-optic folded Mach Zehnder modulator (MZM) that incorporates a waveguide crossing and 3 dB multimode interference couplers for splitting and combining light is reported. The waveguide crossing proves an effective method of realizing a folded modulator, which halves the length of a standard MZM with no penalty to the half wave voltage of the device. This modulator has an effective interaction region length of 10 mm, a physical device length of 6 mm, and shows a DC half wave voltage of roughly 4.0 V, or a modulation efficiency of roughly 4 V·cm, which is measured to be half that of a device with a 5 mm interaction region and no waveguide crossing. Furthermore, the device demonstrates a power extinction ratio of roughly 23 dB, and shows broadband operation with minimal optical sideband power roll-off. Both the low frequency and high frequency data are presented in this work, and, there is a clear path forward to optimizing either or both the low and high frequency operation depending on application-specific requirements. This work demonstrates the functionality of the waveguide crossing in a folded MZM, and proves its effectiveness in decreasing the footprint of such a device.

Funding. Air Force Research Laboratory (FA8650-18-C-1734).

Acknowledgments. This manuscript (AFRL-2022-0029) was supported in part under AFRL contract FA8650-18-C-1734. The authors gratefully acknowledge the support of UTA16-001296. The views and conclusions contained herein are those of the authors and should not be interpreted as necessarily representing the official policies or endorsements, either expressed or implied, of Air Force Research Laboratory, the Department of Defense, or the U.S. Government.

Disclosures. The authors declare that there are no conflicts of interest related to this paper.

Data availability. Data underlying the results presented in this paper are not publicly available at this time but may be obtained from the authors upon reasonable request.

References

1. W. Beardell, B. Mazur, C. J. Ryan, G. J. Schneider, J. Murakowski, and D. W. Prather, "RF-Photonic Spatial-Spectral Channelizing Receiver," J. Lightwave Technol. **40**(2), 432–441 (2021).
2. A. Alvarado, D. J. Ives, S. J. Savory, and P. Bayvel, "On the Impact of Optimal Modulation and FEC Overhead on Future Optical Networks," J. Lightwave Technol. **34**(9), 2339–2352 (2016).
3. Y. Yue, Q. Wang, and J. Anderson, "Experimental Investigation of 400 Gb/s Data Center Interconnect Using Unamplified High-Baud-Rate and High-Order QAM Single-Carrier Signal," Appl. Sci. **9**(12), 2455 (2019).
4. M. Zhang, C. Wang, P. Kharel, D. Zhu, and M. Loncar, "Integrated lithium niobate electro-optic modulators: when performance meets scalability," Optica **8**(5), 652 (2021).
5. M. He, M. Xu, Y. Ren, J. Jian, Z. Ruan, Y. Xu, S. Gao, S. Sun, X. Wen, L. Zhou, L. Liu, C. Guo, H. Chen, S. Yu, L. Liu, and X. Cai, "High-performance hybrid silicon and lithium niobate Mach–Zehnder modulators for 100 Gbit s-1 and beyond," Nat. Photonics **13**(5), 359–364 (2019).

Optics EXPRESS

6. J. Macario, P. Yao, S. Shi, A. Zablocki, C. Harrity, R. D. Martin, C. A. Schuetz, and D. W. Prather, "Full spectrum millimeter-wave modulation," Opt. Express **20**(21), 23623 (2012).
7. P. J. Winzer and D. T. Neilson, "From Scaling Disparities to Integrated Parallelism: A Decathlon for a Decade," J. Lightwave Technol. **35**(5), 1099–1115 (2017).
8. F. Horst, W. M. Green, S. Assefa, S. M. Shank, Y. A. Vlasov, and B. J. Offrein, "Cascaded Mach-Zehnder wavelength filters in silicon photonics for low loss and flat pass-band WDM (de-)multiplexing," Opt. Express **21**(10), 11652 (2013).
9. D. A. B. Miller, "Attojoule Optoelectronics for Low-Energy Information Processing and Communications," J. Lightwave Technol. **35**(3), 346–396 (2017).
10. C. Haffner, W. Heni, Y. Fedoryshyn, J. Niegemann, A. Melikyan, D. L. Elder, B. Baeuerle, Y. Salamin, A. Josten, U. Koch, C. Hoessbacher, F. Ducry, L. Juchli, A. Emboras, D. Hillerkuss, M. Kohl, L. R. Dalton, C. Hafner, and J. Leuthold, "All-plasmonic Mach–Zehnder modulator enabling optical high-speed communication at the microscale," Nat. Photonics **9**(8), 525–528 (2015).
11. E. Wooten, K. Kissa, A. Yi-Yan, E. Murphy, D. Lafaw, P. Hallemeier, D. Maack, D. Attanasio, D. Fritz, G. McBrien, and D. Bossi, "A review of lithium niobate modulators for fiber-optic communications systems," IEEE J. Sel. Top. Quantum Electron. **6**(1), 69–82 (2000).
12. J. Coward, C. Chalfant, and P. Chang, "A photonic integrated-optic RF phase shifter for phased array antenna beam-forming applications," J. Lightwave Technol. **11**(12), 2201–2205 (1993).
13. A. J. Mercante, S. Shi, P. Yao, L. Xie, R. M. Weikle, and D. W. Prather, "Thin film lithium niobate electro-optic modulator with terahertz operating bandwidth," Opt. Express **26**(11), 14810 (2018).
14. A. N. R. Ahmed, S. Nelan, S. Shi, P. Yao, A. Mercante, and D. W. Prather, "Subvolt electro-optical modulator on thin-film lithium niobate and silicon nitride hybrid platform," Opt. Lett. **45**(5), 1112 (2020).
15. A. N. R. Ahmed, S. Shi, A. Mercante, S. Nelan, P. Yao, and D. W. Prather, "High-efficiency lithium niobate modulator for K band operation," APL Photonics **5**(9), 091302 (2020).
16. C. Wang, M. Zhang, X. Chen, M. Bertrand, A. Shams-Ansari, S. Chandrasekhar, P. Winzer, and M. Loncar, "Integrated lithium niobate electro-optic modulators operating at CMOS-compatible voltages," Nature **562**(7725), 101–104 (2018).
17. A. Rao and S. Fathpour, "Compact Lithium Niobate Electrooptic Modulators," IEEE J. Sel. Top. Quantum Electron. **24**(4), 1–14 (2018).
18. G. T. Reed, G. Mashanovich, F. Y. Gardes, and D. J. Thomson, "Silicon optical modulators," Nat. Photonics **4**(8), 518–526 (2010).
19. H. Subbaraman, X. Xu, A. Hosseini, X. Zhang, Y. Zhang, D. Kwong, and R. T. Chen, "Recent advances in silicon-based passive and active optical interconnects," Opt. Express **23**(3), 2487 (2015).
20. S. S. Azadeh, F. Merget, S. Romero-García, A. Moscoso-Mártir, N. von den Driesch, J. Müller, S. Mantl, D. Buca, and J. Witzens, "Low Vπ Silicon photonics modulators with highly linear epitaxially grown phase shifters," Opt. Express **23**(18), 23526 (2015).
21. X. Zhang, C.-J. Chung, A. Hosseini, H. Subbaraman, J. Luo, A. K.-Y. Jen, R. L. Nelson, C. Y.-C. Lee, and R. T. Chen, "High Performance Optical Modulator Based on Electro-Optic Polymer Filled Silicon Slot Photonic Crystal Waveguide," J. Lightwave Technol. **34**(12), 2941–2951 (2016).
22. Oh Min-Cheol, Zhang Hua, and Zhang Cheng, "Recent advances in electrooptic polymer modulators incorporating highly nonlinear chromophore," IEEE J. Sel. Top. Quantum Electron. **7**(5), 826–835 (2001).
23. L. Alloatti, R. Palmer, S. Diebold, K. P. Pahl, B. Chen, R. Dinu, M. Fournier, J.-M. Fedeli, T. Zwick, W. Freude, C. Koos, and J. Leuthold, "100 GHz silicon–organic hybrid modulator," Light: Sci. Appl. **3**(5), e173 (2014).
24. C. Wang, M. Zhang, B. Stern, M. Lipson, and M. Loncar, "Nanophotonic lithium niobate electro-optic modulators," Opt. Express **26**(2), 1547 (2018).
25. A. Rao, A. Patil, P. Rabiei, A. Honardoost, R. DeSalvo, A. Paolella, and S. Fathpour, "High-performance and linear thin-film lithium niobate Mach–Zehnder modulators on silicon up to 50 GHz," Opt. Lett. **41**(24), 5700 (2016).
26. M. Xu, M. He, H. Zhang, J. Jian, Y. Pan, X. Liu, L. Chen, X. Meng, H. Chen, Z. Li, X. Xiao, S. Yu, S. Yu, and X. Cai, "High-performance coherent optical modulators based on thin-film lithium niobate platform," Nat. Commun. **11**(1), 3911 (2020).
27. T. A. Huffman, G. M. Brodnik, C. Pinho, S. Gundavarapu, D. Baney, and D. J. Blumenthal, "Integrated Resonators in an Ultralow Loss Si_3N_4/SiO_2 Platform for Multifunction Applications," IEEE J. Sel. Top. Quantum Electron. **24**(4), 1–9 (2018).
28. S. Jin, L. Xu, H. Zhang, and Y. Li, "$LiNbO_3$ Thin-Film Modulators Using Silicon Nitride Surface Ridge Waveguides," IEEE Photonics Technol. Lett. **28**(7), 736–739 (2016).
29. M. Stocchi, D. Mencarelli, L. Pierantoni, D. Kot, M. Lisker, A. Göritz, C. Baristiran Kaynak, M. Wietstruck, and M. Kaynak, "Mid-infrared optical characterization of thin SiN_x membranes," Appl. Opt. **58**(19), 5233 (2019).
30. A. E. Kaloyeros, F. A. Jové, J. Goff, and B. Arkles, "Review–Silicon Nitride and Silicon Nitride-Rich Thin Film Technologies: Trends in Deposition Techniques and Related Applications," ECS J. Solid State Sci. Technol. **6**(10), P691–P714 (2017).
31. T. Ren, M. Zhang, C. Wang, L. Shao, C. Reimer, Y. Zhang, O. King, R. Esman, T. Cullen, and M. Loncar, "An integrated low-voltage broadband lithium niobate phase modulator," IEEE Photonics Technol. Lett. **31**(11), 889–892 (2019).

Optics EXPRESS

32. D. Khalil and A. Yehia, "Two-dimensional multimode interference in integrated optical structures," J. Opt. A: Pure Appl. Opt. **6**(1), 137–145 (2004).
33. J. Wang, M. Qi, Y. Xuan, H. Huang, Y. Li, M. Li, X. Chen, Q. Jia, Z. Sheng, A. Wu, W. Li, X. Wang, S. Zou, and F. Gan, "Proposal for fabrication-tolerant SOI polarization splitter-rotator based on cascaded MMI couplers and an assisted bi-level taper," Opt. Express **22**(23), 27869 (2014).
34. J. A. Ibarra Fuste and M. C. Santos Blanco, "Bandwidth–length trade-off figures of merit for electro-optic traveling wave modulators," Opt. Lett. **38**(9), 1548 (2013).